Spectroscopic Constraints on the Buildup of Intracluster Light in the Coma Cluster

The Astrophysical Journal, 894:32 (16pp), 2020 May 1 https://doi.org/10.3847/1538-4357/ab845c

Spectroscopic Constraints on the Buildup of Intracluster Light in the Coma Cluster

Meng Gu[1,2], Charlie Conroy[1], David Law[3], Pieter van Dokkum[4], Renbin Yan[5], David Wake[6], Kevin Bundy[7], Alexa Villaume[7], Roberto Abraham[8], Allison Merritt[9], Jielai Zhang[10], Matthew Bershady[11,12], Dmitry Bizyaev[13,14], Niv Drory[15], Kaike Pan[13], Daniel Thomas[16], and Anne-Marie Weijmans[17]
[1] Department of Astronomy, Harvard University, Cambridge, MA 02138, USA
[2] Department of Astrophysical Sciences, Princeton University, Princeton, NJ 08544, USA
[3] Space Telescope Science Institute, 3700 San Martin Drive, Baltimore, MD 21218, USA
[4] Astronomy Department, Yale University, New Haven, CT 06511, USA
[5] Department of Physics and Astronomy, University of Kentucky, 505 Rose Street, Lexington, KY 40506-0057, USA
[6] Department of Physical Sciences, The Open University, Milton Keynes, MK7 6AA, UK
[7] Department of Astronomy and Astrophysics, University of California, Santa Cruz, CA 95064, USA
[8] Department of Astronomy and Astrophysics, University of Toronto, 50 St. George Street, Toronto, ON M5S 3H4, Canada
[9] Max-Planck-Institut für Astronomie, Königstuhl 17, D-69117 Heidelberg, Germany
[10] Schmidt Science Fellows, in Partnership with the Rhodes Trust, Rhodes House, Oxford, OX1 3RG, UK
[11] Department of Astronomy, University of Wisconsin-Madison, 475N. Charter Street, Madison, WI 53703, USA
[12] South African Astronomical Observatory, P.O. Box 9, Observatory 7935, Cape Town, South Africa
[13] Apache Point Observatory, P.O. Box 59, Sunspot, NM 88349, USA
[14] Sternberg Astronomical Institute, Moscow State University, Moscow, Russia
[15] McDonald Observatory, The University of Texas at Austin, 1 University Station, Austin, TX 78712, USA
[16] Institute of Cosmology & Gravitation, University of Portsmouth, Dennis Sciama Building, Portsmouth, PO1 3FX, UK
[17] School of Physics and Astronomy, University of St. Andrews, North Haugh, St. Andrews KY16 9SS, UK
Received 2018 October 29; revised 2020 March 6; accepted 2020 March 24; published 2020 May 1

Abstract

The stellar content of the intracluster light (ICL) provides unique insight into the hierarchical assembly process of galaxy clusters. We present optical spectra of three ICL regions ($\mu_g \approx 25.3$–26.2 mag arcsec^{-2}) in the Coma cluster, located between 100 and 180 kpc from their nearest brightest cluster galaxies (BCGs): NGC 4889 and NGC 4874. Integral-field unit (IFU) spectroscopy with 13.5 hr on-source integration was acquired in an ancillary program within the Sloan Digital Sky Survey-IV MaNGA survey. We stacked the 127 individual fiber spectra in each IFU to achieve a 1σ limiting surface brightness of 27.9 mag arcsec^{-2}, corresponding to a mean signal-to-noise ratio in the optical of 21.7, 9.0, and 11.7 Å^{-1}, for each ICL region. We apply stellar population models to the stacked spectra. Our results show that the velocity dispersions of ICL regions are very high ($\sigma \sim 630$ km s^{-1}), indicating the stars in these regions are tracing the gravitational potential of the cluster, instead of any individual galaxy. The line-of-sight velocities are different from each other by ~700 km s^{-1}, while the velocity of each region is similar to the closest BCG. This suggests that the ICL regions are associated with two distinct subclusters centered on NGC 4889 and NGC 4874. The stellar populations of these regions are old and metal-poor, with ages of $12.7^{+1.0}_{-3.4}$, $6.7^{+2.9}_{-2.0}$, and $9.7^{+3.5}_{-3.5}$ Gyr, and [Fe/H] of $-1.0^{+0.2}_{-0.3}$, $-0.6^{+0.3}_{-0.5}$, and $-0.8^{+0.3}_{-0.4}$. From the derived age and metallicity, the buildup of ICL in Coma is likely to be through the accretion of low-mass galaxies or the tidal stripping of the outskirts of massive galaxies that have ended their star formation early on, instead of directly from major mergers of massive galaxies.

Unified Astronomy Thesaurus concepts: Coma Cluster (270); Galaxy evolution (594)

1. Introduction

According to the widely accepted Λ Cold Dark Matter model, massive early type galaxies (ETGs) are assembled hierarchically following their underlying dark matter structures (White & Rees 1978). The evolution of ETGs in massive halos can be described by a two-phase picture (Naab et al. 2007; Feldmann et al. 2010; Oser et al. 2010, 2012; Johansson et al. 2012; Lackner et al. 2012; Navarro-González et al. 2013; Rodriguez-Gomez et al. 2016; Qu et al. 2017): at high redshift, their evolution is dominated by the concentrated mass growth through rapid dissipational *in situ* star formation (Daddi et al. 2005; Trujillo et al. 2006; Hopkins et al. 2008; Dekel et al. 2009; Hyde & Bernardi 2009) At later times, their evolution is increasingly dominated by the buildup of the outskirts through multiple mergers and accretions of lower-mass galaxies (Ostriker & Tremaine 1975; Bezanson et al. 2009; van Dokkum et al. 2010; van der Wel et al. 2011, 2014).

Brightest cluster galaxies (BCGs) are a special class of ETGs residing near the center of galaxy clusters. The most significant structural feature of BCGs is their diffuse and extended stellar envelopes, so they are also classified as cD galaxies. If we trace the stellar distribution from the inner regions of BCGs to the stellar envelopes, part of the stellar components would no longer be bound to the galaxy, but instead would be associated with the whole cluster as we approach large radius. Many studies have confirmed that, in some massive ETGs and BCGs, the stellar velocity dispersion profiles rise with increasing radii toward the velocity dispersion of the cluster (e.g., Faber et al. 1977; Dressler 1979; Kelson et al. 2002; Bender et al. 2015; Veale et al. 2018). The stellar structure surrounding BCGs that are gravitationally bound to the galaxy cluster is called the intracluster light (ICL; Zwicky 1951). The formation of the ICL is considered to be a combined effect of multiple mechanisms, including tidal disruption of dwarf galaxies (Rudick et al. 2009), tidal stripping through galaxy interactions (Gregg & West 1998; Calcáneo-Roldán et al. 2000; Conroy et al. 2007; Purcell et al. 2007; Rudick et al. 2009; Contini et al. 2014), violent relaxation during major mergers (Murante et al. 2007;

Contini et al. 2018), and *in situ* star formation (Puchwein et al. 2010). Stellar populations in the outskirts of galaxies and the ICL, if measured, can help constrain these scenarios.

Observing the outskirts of massive ETGs is difficult due to the low surface brightness, but this field has been accelerated by state-of-the-art instruments and improved data reduction in both photometry (Mihos et al. 2005; van Dokkum et al. 2014; Duc et al. 2015; Huang et al. 2016, 2018a, 2018b) and spectroscopy (Sánchez-Blázquez et al. 2007; Foster et al. 2009; Coccato et al. 2010, 2011; Spolaor et al. 2010; Greene et al. 2012, 2015). Observations of the diffuse ICL with extremely low surface brightness is even more challenging. Deep imaging and accurate sky subtraction are required to detect the ICL and constrain its growth over time (Gonzalez et al. 2005; Mihos et al. 2005; Zibetti et al. 2005; Rudick et al. 2010; Toledo et al. 2011; Guennou et al. 2012; Giallongo et al. 2014; Burke et al. 2015). The stellar population and kinematic properties have been explored through multiwavelength photometry (Williams et al. 2007; Montes & Trujillo 2014, 2018), integral-field spectroscopy (Adami et al. 2016; Edwards et al. 2016), globular clusters (Alamo-Martínez & Blakeslee 2017), and individual objects such as planetary nebulae (Arnaboldi et al. 2003, 2004; Feldmeier et al. 2004; Gerhard et al. 2007) and red giant branch stars (Williams et al. 2007; Longobardi et al. 2015).

In this paper, we present a stellar population analysis from the BCG centers out to the ICL regime through full spectral modeling, and provide the recession velocity, velocity dispersion, stellar age, and iron abundance out to 180 kpc. This is the first time that the stellar population analysis through full optical spectra modeling is performed beyond 100 kpc. We make use of the data obtained as part of the Deep Coma ancillary program within the Sloan Digital Sky Survey (SDSS)-IV/MaNGA program, and the *g*- and *r*-band photometry from the Dragonfly Telephoto Array (Abraham & van Dokkum 2014). The Coma cluster has a median redshift of $cz = 7090\,\mathrm{km\,s^{-1}}$ (Geller et al. 1999) and a velocity dispersion of $\sigma \sim 1000\,\mathrm{km\,s^{-1}}$ (Colless & Dunn 1996; Mobasher et al. 2001; Rines et al. 2013; Sohn et al. 2016). The distance of the Coma Cluster is assumed to be 100 Mpc, adopted from Liu & Graham (2001). This corresponds to a distance modulus of 35.0 mag and a scale of 0.474 kpc $\mathrm{arcsec^{-1}}$. The Galactic foreground extinction for Coma Cluster is $A_g = 0.030$ mag and $A_r = 0.021$ mag (Schlafly & Finkbeiner 2011).

2. Data

2.1. Project Overview and Observation Strategy

We make use of data obtained by the MaNGA (Mapping Nearby Galaxies at Apache Point Observatory) Survey (Bundy et al. 2015; Yan et al. 2016; Drory et al. 2015; Wake et al. 2017; Abolfathi et al. 2018). MaNGA is a large, optical integral field spectroscopy survey with 17 deployable integral field units (IFUs) ranging from 12″ to 32″ in diameter. It is one of the fourth-generation Sloan Digital Sky Survey (SDSS-IV) programs (Gunn et al. 2006; Blanton et al. 2017). The primary goal of MaNGA is to obtain integral field spectroscopy of ∼10,000 nearby galaxies.

MaNGA utilizes IFUs from two dual-beam Baryonic Oscillation Spectroscopic Survey (BOSS) spectrographs (Drory et al. 2015) that are on the SDSS 2.5 m telescope. The spectrographs have 1423 fibers in total, which are bundled into different sizes of IFUs. The diameter of each fiber is 1.″98 on the sky. The wavelength coverage of the spectrographs is 3622–10354 Å with a ∼400 Å overlap from ∼5900 to ∼6300 Å between the blue and red cameras. The spectral resolution is $R = 1560$–2650.

Our data come from one of the MaNGA's ancillary programs, the Coma Deep program (also see Gu et al. 2018b). This is the deepest MaNGA ancillary program, consisting of six plates designed to observe specially selected targets in the Coma cluster. The goal of the Coma Deep program is to study the stellar population of various kinds of targets in the Coma cluster and its surrounding area. The plates are ∼0.7 m in diameter and 3° on the sky. The center of all plates is at R.A. $= 12^{\mathrm{h}}58^{\mathrm{m}}35\overset{\mathrm{s}}{.}58$, decl. $= 27^{\mathrm{d}}36^{\mathrm{m}}12\overset{\mathrm{s}}{.}744$. Five massive ETGs are selected for observations: NGC 4889, NGC 4874, NGC 4860, NGC 4839, and NGC 4841A. Three dwarf elliptical galaxies are also selected: GMP 2232, GMP 5076, and GMP 5361. Observations of massive ETGs are conducted on their central regions and outskirts up to ∼40 kpc away from the centers. These positions are carefully chosen for optimizing IFU bundle mapping of desired targets. Three 127-fiber bundles are placed in regions of extremely low surface brightness in order to probe the stellar populations of the ICL. These regions are selected based on deep images by the Dragonfly Telephoto Array and are away from any foreground contamination, with a surface brightness in the *g* band from 25.3 to 26.2 mag $\mathrm{arcsec^{-2}}$. The pipeline and data reduction process of the Dragonfly images are described in Jielai Zhang's PhD thesis.[18] The diameter of each 127-fiber IFU bundle on the sky is 32.″5.

Locations of IFU bundles on two BCGs and three ICL regions are shown in the Dragonfly *g*-band surface brightness map in Figure 1. The distances from ICL1 to NGC 4889 and NGC 4874 are 219.″2 and 219.″6, respectively. The distances from ICL2 and ICL3 to NGC 4874 are 382.″1 and 332.″7, respectively.

Two 127-fiber IFUs are used to observe NGC 4889 and NGC 4874. We observed their central regions on the first and second Coma plates. Corresponding bundles in the third and fourth plates are used to observe regions about $1R_e$ and $0.5R_e$ from the centers of NGC 4889 and NGC 4874. They are located 39.″0 and 34.″5 from the centers, respectively. IFU bundles are placed at $2R_e$ of NGC 4889 and $1R_e$ of NGC 4874 in the fifth and sixth plates. Their locations are 71.″5 and 66.″7 from the centers, respectively. The regions are chosen to best avoid contamination from nearby sources. A similar strategy is adopted for NGC 4860, NGC4839, and NGC 4841A. They are observed by 91 fiber and 61 fiber bundles. Three dwarf elliptical galaxies, GMP 2232, GMP 5076, and GMP 5361 are observed by 37 fiber bundles. The locations of IFU bundles on ICL and dwarf elliptical galaxies are kept the same throughout the six plates, providing the deepest MaNGA observations on single targets.

Because the dark-time sky background at the Apache Point Observatory is ∼22 mag $\mathrm{arcsec^{-2}}$ in *g*-band, excellent sky subtraction is required to probe regions with low surface brightness. In Deep Coma plates, the locations of reference sky fibers are carefully selected using broadband images taken by the Dragonfly Telephoto Array, reaching a *g*-band surface brightness $\mu_g > 27.8$ mag $\mathrm{arcsec^{-2}}$ for sky fiber locations

[18] https://jielaizhang.github.io/files/Zhang_Jielai_201811_PhD_Thesis_excludech4.pdf

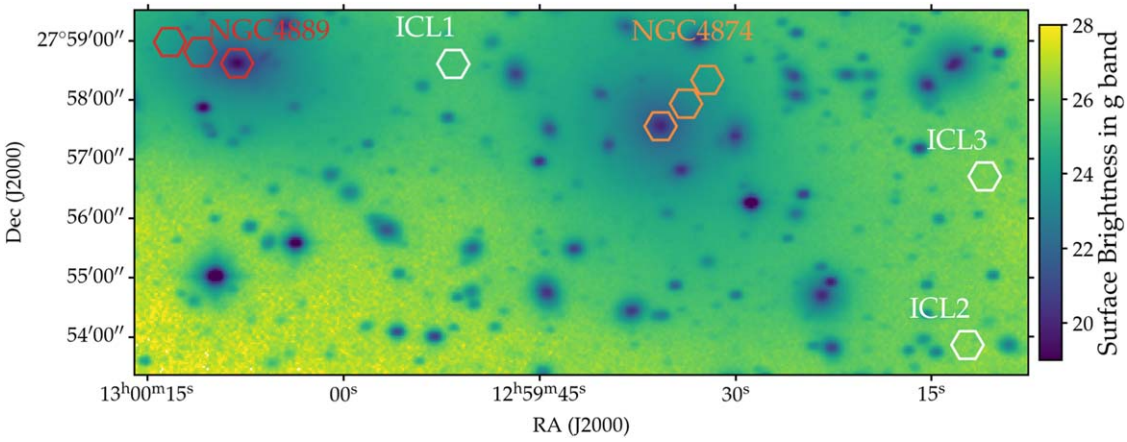

Figure 1. Overview of the IFU bundle locations on the *g*-band surface brightness map observed by the Dragonfly Telephoto Array. Red hexagons show IFU locations on the center, $1R_e$, and $2R_e$ of NGC 4889. Orange hexagons show IFU locations on the center, $0.5R_e$, and $1R_e$ of NGC 4874. White hexagons show locations of IFUs on ICL1, ICL2, and ICL3, respectively.

(∼3″ around each fiber) based on the Dragonfly imaging. In addition to the 92 single fibers used to construct the model sky spectrum for ordinary MaNGA plates, three IFU bundles (two 19 fiber bundles, one 37 fiber bundle) were devoted to additional measurements of the sky, hence there are 167 sky fibers in total used across both spectrographs.

In addition, we adopt an on-and-off nodding strategy to improve the accuracy of the background estimate and to mitigate systematics. By shifting the whole field approximately 20′ away, we obtain reference "all-sky" exposures, during which a large fraction of the sky fibers and science IFUs sample the blank sky. Each of the first two plates includes nine 5 minute nodded sky exposures at nine different locations between the normal science exposures. After the first two plates, we decided to change the exposure time to the same as that of the science exposure, in order to better constrain the systematics. Therefore, each of the last four plates includes four 15 minute nodded sky exposures at four different locations.

2.2. Data Reduction

We processed the data using a custom modified version of the MaNGA Data Reduction Pipeline MPL-8 (DRP; Law et al. 2015, 2016). Compared to MPL-7, which is publicly available in Data Release 15 (DR15),[19] MPL-8 offers several improvements in MaNGA pipeline, including procedures related to astrometry and flux calibration. The baseline DRP first removes detector overscan regions and quadrant-dependent bias and extracts the spectrum of each fiber using an optimal profile-fitting technique. It uses the sky fibers to create a supersampled model for the background sky spectrum and subtracts this model spectrum from each of the science fibers. Flux calibration is then performed on individual exposures using twelve 7 fiber IFUs targeting spectrophotometric standard stars (Yan et al. 2016, 2016). Fiber spectra from the blue and red cameras are then combined together onto a common logarithmic wavelength solution using a cubic b-spline fit. We make use of MaNGA data in two formats in this work. The "mgSFrame" files are data set including the spectra after fiber extraction and sky subtraction in each exposure and camera. The "mgCFrame" files provide spectra after flux calibration. In addition, the blue and red cameras are stitched together across the dichroic break. Fibers from two spectrographs are combined as well. As a result, the "mgCFrame" files represent spectra of all 1423 MaNGA fibers from a single exposure in a row-stacked format, where each row corresponds to an individual one-dimensional fiber spectrum. The logarithmic wavelength grid runs from $\log\lambda(\text{Å}) = 3.5589$ to $\log\lambda(\text{Å}) = 4.0151$, which corresponds to 4563 spectral elements from 3621.5960 to 10353.805 Å. In this paper, we only use the data taken by the blue spectrograph, which covers the wavelength range from 3600 to 6300 Å, with a short range from 5900 to 6300 Å overlap with the red spectrograph. This allows us to avoid additional issues associated with the numerous bright atmospheric OH features in the red.

As described in Gu et al. (2018b), our analysis is possible only with exquisite control of detector and instrumental systematics, and therefore some changes to the DRP have been made specifically for the Deep Coma program. Analysis of our nodded all-sky observations showed evidence for low-level systematics in the detector electronics. Therefore, we added a step to measure and remove a $0.5\,e^-$ pixel^{-1} offset in bias between the light-sensitive detector pixels and the overscan region, compensating at the same time for a seasonally dependent $0.1\,e^-$ pixel^{-1} drift in the difference. In addition, the amplifier-dependent gain values tended to drift from one exposure to the next away from nominal at the ∼0.1% level; we added procedures to measure and correct for this effect empirically using the sky fibers in each exposure. Finally, we modified the DRP to be able to apply the flux calibration vector from the nearest ordinary science exposure in time to the nod exposures (for which there are no calibration stars in the 7 fiber mini-bundles).

In addition, performance analysis of early observations in the Deep Coma program revealed that scattered light and the extended (>100 pixel) profile wings of bright galaxies targeted by the Coma program were contaminating the spectra of fainter objects. We therefore redesigned our observing program to consolidate all bright targets (ETGs and dwarf ellipticals) onto one of the two BOSS spectrographs (Smee et al. 2013) and all faint targets (UDGs and ICL) onto the other, so that these targets never share a detector.

Although these modifications substantially improve performance for the Deep Coma program relative to the standard DRP, we find that the final stacked science spectra are

[19] https://www.sdss.org/dr15/

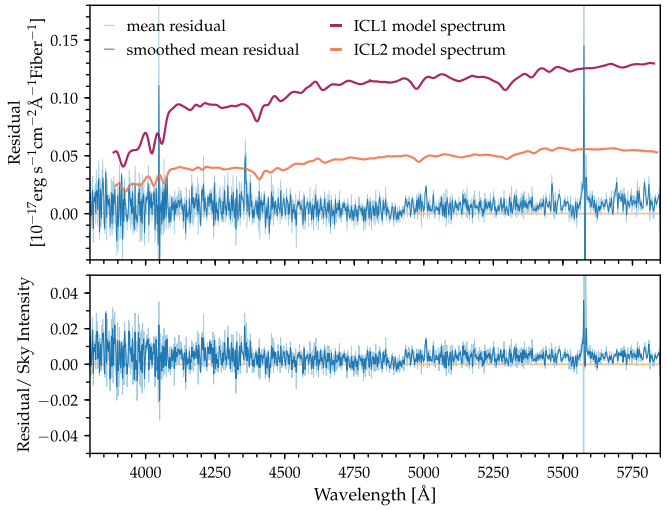

Figure 2. Top panel: mean stacked residual of sky-subtracted sky spectra from all science fibers in the nod exposures in which all bundles are placed on background sky (light blue), and that smoothed by a 3 pixel moving box (dark blue). Model spectra of the brightest (ICL1, red) and faintest (ICL2, orange) ICL regions are shown as a noiseless version of the expected target flux level. Description of model spectra can be found in Section 3. Bottom panel: fractional residual relative to the sky intensity.

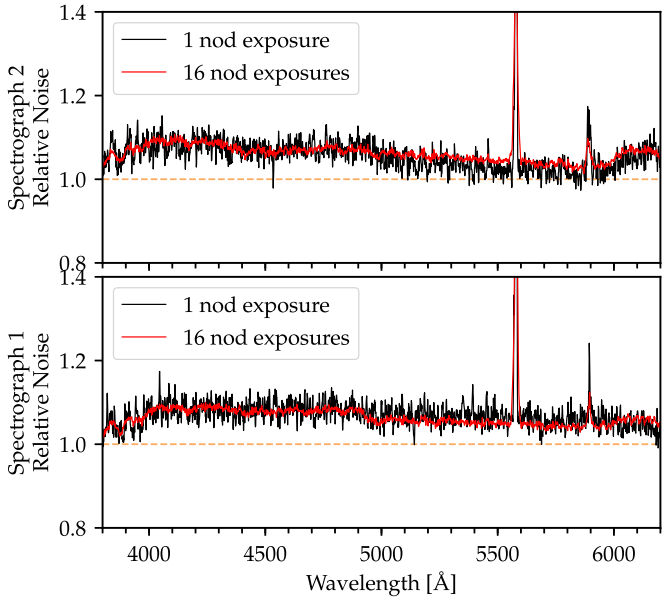

Figure 3. Ratio between the actual noise and the expected noise from the detector read noise and Poisson counting statistics as a function of wavelength for the science spectra in one sky-subtracted nod exposure (black), and that in all 16 nod exposures (red). Top and bottom panels show results in the first and second spectrographs, respectively. Relative noise of 1.0 means perfect, "Poisson limited" sky subtraction (dotted line).

nonetheless still limited by systematic residuals over wavelength scale >100 Å. These residuals are consistent between stacked science and nodded sky spectra within each plate, possibly due to cartridge-dependent uncertainties in fiber alignment and the detector point-spread function. The offset ranges from 0 to 1 $\times$ 10^{-18} erg s^{-1} cm^{-2} Å $^{-1}$. In the last four plates, we mitigate the impact of these systematics by fitting the stacked spectra of the sky-subtracted nodded sky exposures with a 3 degree polynomial from 3836 to 5873 Å in the observed frame and subtracting the result from the corresponding science exposures prior to stacking science spectra. The amplitude of the polynomial correction ranges from 10^{-19} to 10^{-18} erg s^{-1} cm^{-2} Å^{-1} in the continuum, and represents an important correction to the baseline flux level for extremely faint targets. We match the continuum levels of stacked spectra from different plates via subtracting the above polynomial continuum before we derive any science result.

2.3. Sky Subtraction Performance

We make use of the nodded sky exposures to test the sky subtraction performance we can achieve for the spatially stacked ICL spectra. We perform the same analysis on the 15 minute nodded sky exposures in the last four Deep Coma plates, and spatially stack the sky-subtracted sky spectral from all science fibers in these 16 exposures. This provides an estimate of the sky residual. Figure 2 shows the sky-subtracted residual (top panel), and the fractional residual relative to the sky intensity (bottom panel) from the stacked sky-subtracted spectra in nodded sky exposures. Since the number of Deep Coma science exposures is roughly 3$\times$ the number of nodded sky exposures, the residuals are smoothed by a 3 pixel moving box to mimic the residual we could achieve by stacking the same number of nodded sky exposures as the science exposures. They are shown as the dark blue lines. The residuals are very close to zero in the 3800–5800 Å wavelength range we used to perform the stellar population analysis. The fractional residual relative to the sky intensity is, on average, within 1%. We further compare the flux level of our science targets by including model spectra of ICL1 and ICL2 as a noiseless version of the expected flux level. The description of model spectra can be found in Section 3. ICL1 and ICL2 are the brightest and faintest ICL regions, respectively. Figure 2 shows that ICL1 has a flux level much higher than the sky residuals, about 9$\times$ the mean sky residual in the 3800–5800 Å. In general, ICL2 is above the mean stacked residual (4$\times$) except for the bright sky lines, which are masked out during our spectral fitting procedure.

We also examine whether the sky subtraction is "Poisson limited" by constructing "Poisson ratio" images following the procedures described in Law et al. (2016). The inverse variance in the "mgSFrame" spectra represents the combined effect of shot noise and detector read noise. By comparing the distribution of the sky-subtracted residual with the expected noise from the detector read noise and Poisson counting statistics, we are able to evaluate the sky-subtraction performance in single and multiple exposures. As shown in Figure 3, the distribution of the Poisson ratio is slightly above 1.0, but on average is smaller than 1.1 at all wavelengths, except for the few strongest sky lines. Stacking across multiple exposures does not increase this ratio.

Further, we calculate the 1σ limiting surface brightness following the steps in Law et al. (2016). Using the flux-calibrated, camera-combined mgCFrame spectra, we calculate the limiting 1σ surface brightness in 4000–5500 Å achieved in the blank sky by randomly stacking different numbers of spectra. The results are shown in Figure 4. For a typical MaNGA all-sky exposure with 92 available sky fibers (red), the performance is limited by the number of sky fibers, and therefore decreases as $\sqrt{N^{-1} + 92^{-1}}$. For a Coma nodded exposure, there are 167 sky fibers, therefore the 1σ limiting surface brightness (blue) follows the curve of $\sqrt{N^{-1} + 167^{-1}}$.

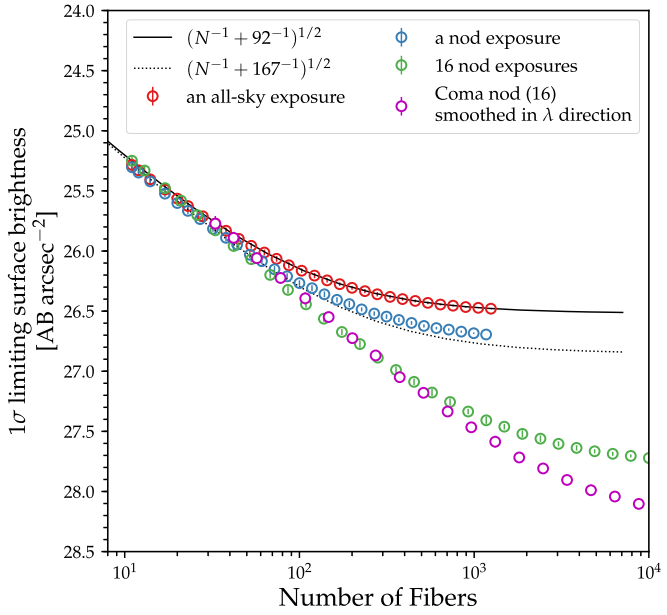

Figure 4. The 1σ limiting surface brightness in the wavelength range 4000–5500 Å as a function of the number of randomly selected and combined fibers in a standard MaNGA all-sky exposure (92 sky fibers; red), a Deep Coma nod exposure (167 sky fibers; blue), and 16 nod exposures (green). Solid and dotted black lines show the theoretical expectation based on $\sqrt{N^{-1}+92^{-1}}$ for an all-sky exposure and $\sqrt{N^{-1}+167^{-1}}$ for a nod exposure, respectively. Performance of stacking across all 54 science exposures (purple) is estimated by smoothing the stacked spectrum of all 16 nod exposures by a factor of 3 in the wavelength direction. Sky level in all exposures is ∼22 mag arcsec^{-2}.

Stacking across different exposures is more complicated, and we estimate this performance by stacking across all 16 Coma nod exposures (green). We further smoothed the stacked nod exposures in the wavelength direction by a factor of 3 in order to mimic the 1σ limiting surface brightness we are able to achieve via 54 science exposures, which have ∼3× exposures as the nod exposures. With the same number of science fibers as we used in our ICL targets, the 1σ limiting surface is about 28 mag arcsec^{-2}. Finally, we estimate the 1σ limiting surface brightness achieved by stacking all ICL1 fibers in all 54 exposures by first subtracting off a high smoothed continuum model in each spectrum. The 1σ limiting surface brightness derived from ICL1, 27.9 mag arcsec^{-2}, is a close estimate of the real performance, and is roughly consistent with the predictions from the nodding exposures. Since the surface brightness of three ICL regions is $\mu_g \approx$ 25.3–26.2, they are about at the same level of 10σ limiting surface brightness. In summary, we achieve a 1σ limiting surface brightness of 27.9 mag arcsec^{-2} by spatially stacking the ICL spectra over 54 science exposures for our $\mu_g \approx$ 25.3–26.2 mag arcsec^{-2} targets under the $\mu_g \approx$ 22 mag arcsec^{-2} sky background.

3. Stellar Population Modeling

3.1. Absorption Line Fitter

Our main tool for modeling spectra of galaxies and ICL in our sample is the absorption line fitter (`alf`; Conroy & van Dokkum 2012; Conroy et al. 2014, 2017, 2018). Using `alf` enables stellar population modeling of the full spectrum for stellar ages >1 Gyr and for metallicities from ∼−2.0 to +0.25. With `alf`, we explore the parameter space using a Markov chain Monte Carlo (MCMC) algorithm (`emcee`; Foreman-Mackey et al. 2013). The program now adopts the MIST stellar isochrones (Choi et al. 2016) and utilizes a new spectral library that includes continuous wavelength coverage from 0.35 to 2.4 μm over a wide range in metallicity. This new library, described in Villaume et al. (2017), is the result of obtaining new IRTF NIR spectra for stars in the MILES optical spectral library (Sánchez-Blázquez et al. 2006). Finally, theoretical response functions, which tabulate the effect on the spectrum of enhancing each of 18 individual elements, were computed using the ATLAS and SYNTHE programs (Kurucz 1970, 1993). Further details of these updates to `alf` are described in Conroy et al. (2018). With `alf`, we are able to fit a two-burst star formation history, the redshift, velocity dispersion, overall metallicity ([Z/H]), 18 individual element abundances, several initial mass function (IMF) parameters, and a variety of "nuisance" parameters.

Throughout this paper, we use `alf` in a simplified mode. Not all the parameters are included, but only the recession velocity, age, overall metallicity [Z/H], and abundances of Fe, C, N, O, Mg, Si, Ca, Ti, and Na. The IMF is fixed to the Kroupa (2001) form. Instead of adopting a two-burst star formation history in the standard model, the simplified mode adopts only a single age component. We adopt this approach due to the limited signal-to-noise ratio (S/N) of the data. We adopt flat priors from 500 to 10,500 km s^{-1} for recession velocity, 10–2000 km s^{-1} for velocity dispersion, 1.0–14.0 Gyr for age, and −1.8 − +0.3 for [Fe/H]. The priors are zero outside these ranges. For each spectrum, we normalize the continuum by fitting the ratio between model and data in the form of a polynomial. For spectra from IFU bundles that are located within 50 kpc from the centers of BCGs, we use the polynomial with order of ($\lambda_{\rm max}$–$\lambda_{\rm min}$)/100 Å. For ICL targets, due to the large velocity dispersion in the stellar content, we adopt a sixth-order polynomial (see Appendix). For each likelihood evaluation, the polynomial-divided input spectra are matched with the model. Normalization occurs in two separate wavelength intervals, 3800–4700 Å and 4700–5600 Å. Pixels near bright sky lines in the blue were masked prior to the fitting.

Figure 5 shows model spectra for old and low-metallicity stellar populations with the same stellar age of 10 Gyr and [Fe/H] of −0.7, but different velocity dispersions: 200, 400, and 600 km s^{-1}. For a typical ETG, the velocity dispersion in the central region is roughly 200–300 km s^{-1}. The velocity dispersions in the ICL regions are >400 km s^{-1}. Compared to typical ETGs, the stellar absorption features in regions with >400 km s^{-1} become much shallower with increasing velocity dispersion. Therefore, ICL spectra are noticeably different than typical ETG spectra.

4. Results

4.1. Stellar Population of the ICL

We now present our results from full spectra modeling. The total on-source exposure time for each ICL regions is 13.5 hours. The mean S/N ratios we achieved for ICL1, ICL2, and ICL3 in a wavelength range from 4500 to 5000 Å are 21.7, 9.0, and 11.7 Å^{-1}. Figure 6 shows the median stacked spectra for ICL1, ICL2, and ICL3 from the 54 15 minute exposures observed by the six Coma plates (Plate 8479, 8480, 8953, 9051). The spectra shown in the figure are smoothed by a

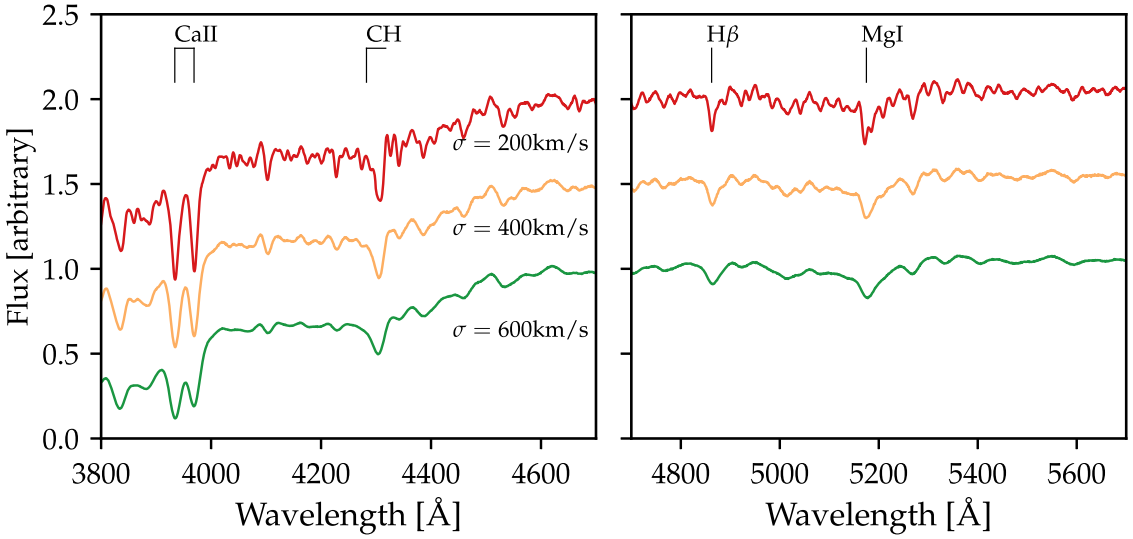

Figure 5. Model spectra for stellar populations of age 10 Gyr and [Fe/H] = –0.7 with different velocity dispersions. Spectra in red, orange, and green are smoothed with velocity dispersions of 200, 400, and 600 km s^{-1}, respectively. Targets with high velocity have much shallower absorption features. Prominent absorption features in the ICL spectra are labeled.

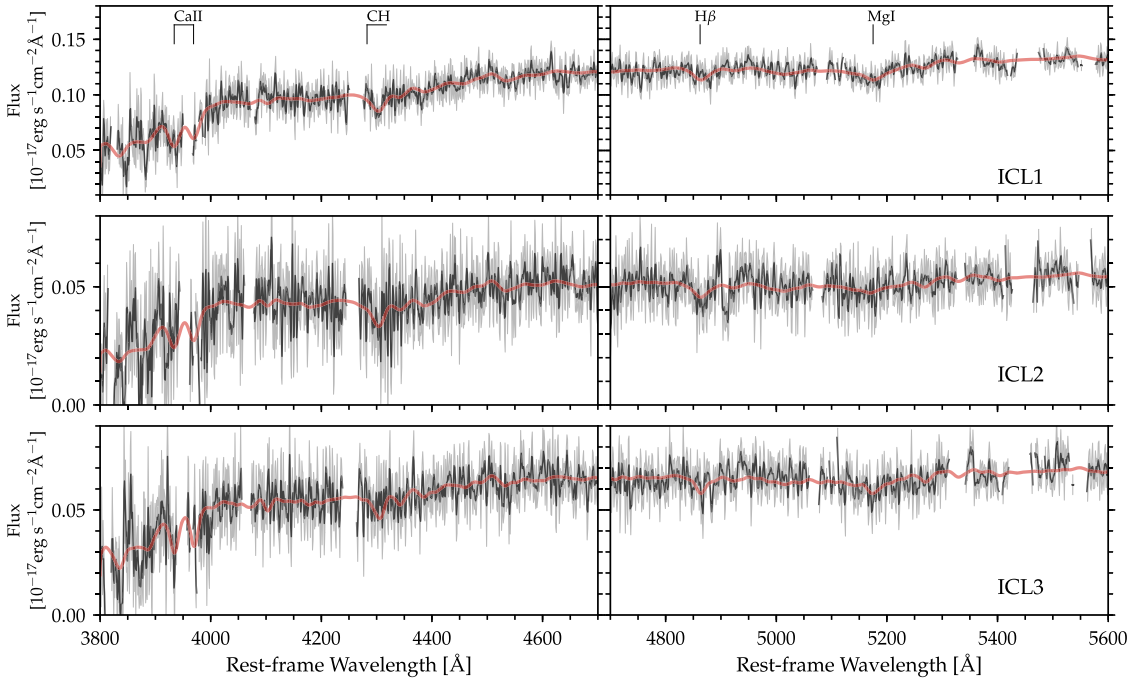

Figure 6. Stacked spectra (black) and best-fit model spectra (red) with parameters at minimum χ^2 from `alf` of ICL1 (top), ICL2 (middle), and ICL3 (bottom). Spectra are smoothed with a 3 pixel boxcar filter for the purpose of better display. Gray shaded regions show the uncertainty of flux from the input spectra. Gaps in the black lines indicate pixels that are masked prior to the fitting, which are pixels contaminated by bright sky lines.

3 pixel boxcar kernel. Visually prominent stellar absorption features for old stellar populations have been captured by the best-fit model spectra (red), including Ca II H and K lines, CH, Hβ, and Mg I. The red spectra show the spectra best fit by `alf` at minimum χ^2.

In Figure 7, we show the projections of posteriors (Foreman-Mackey 2016) for four parameters: recession velocity (cz), velocity dispersion, log(age), and [Fe/H]. The posterior distributions are well-approximated by a Gaussian. Dashed lines show the values of parameters at the 16th, 50th, and 84th percentiles of posteriors. Blue lines mark the values of parameters at minimum χ^2. Outliers are shown as dots. We note that both the best-fit model spectra and the posterior distributions provide important information about our model. The 2D projections of posteriors are present to reflect the uncertainties and degeneracy among the model parameters. The best-fit model spectra and the posterior distributions should be interpreted together as the best constrained values, given the current model assumption and data quality.

The Coma cluster has a median redshift of $cz = 7090\,\mathrm{km\,s^{-1}}$ (Geller et al. 1999). The recession velocities of ICL1, ICL2, and ICL3 are $6760^{+141}_{-37}\,\mathrm{km\,s^{-1}}$, $7252^{+79}_{-115}\,\mathrm{km\,s^{-1}}$,

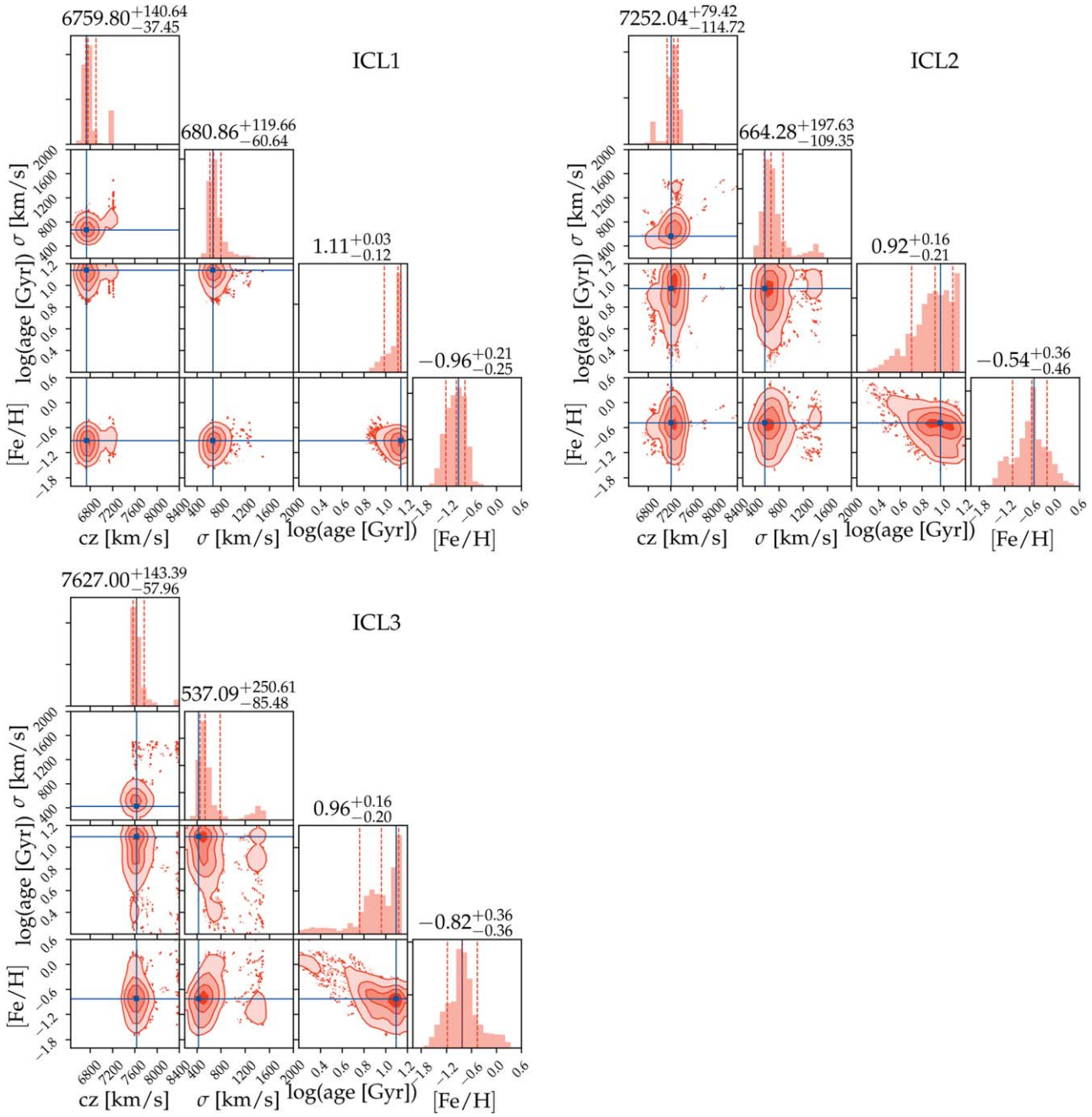

Figure 7. Projections of the posterior of recession velocity, velocity dispersion, log(age), and [Fe/H] from `alf` in 1D and 2D histograms for ICL1, ICL2, and ICL3. Dashed lines and contours show the 16th, 50th, and 84th percentiles of posteriors. Blue lines represent the best-fit parameters at $\chi^2_{\rm min}$, which are used to generate best-fit model spectra.

and 7627^{+143}_{-58} km s^{-1}, respectively. The derived velocity dispersions confirm that the stellar contents in these regions belong to the Coma cluster. All of the three ICL regions have high velocity dispersion: 681^{+120}_{-61}, 664^{+198}_{-109}, 537^{+251}_{-85} km s^{-1}. The stellar ages of ICL1, ICL2, and ICL3 are $12.9^{+0.9}_{-3.2}$ Gyr, $8.3^{+3.8}_{-3.2}$ Gyr, and $9.1^{+4.0}_{-3.4}$ Gyr, respectively. The iron abundances, [Fe/H], are $-0.96^{+0.21}_{-0.25}$, $-0.54^{+0.36}_{-0.36}$, and $-0.82^{+0.36}_{-0.36}$, respectively. The stellar populations in all three ICL regions are old and more metal-poor compared to the inner regions of their nearby massive ETGs. Both the low metallicity and large velocity dispersion lead to less significant absorption features, making it more difficult to extract stellar population properties (see Appendix for more detail).

4.2. Surface Brightness and Color Profiles

We derive the surface brightness profiles of NGC 4889 and NGC 4874 by performing the `IRAF`[20] task `ELLIPSE` (Jedrzejewski 1987) on the sky-subtracted Dragonfly images. Surrounding objects are aggressively masked iteratively using `SExtractor` (Bertin & Arnouts 1996). The centers of galaxies are determined first, then the ellipticity and position angle are determined by the median values in radial range 10–100 kpc. We extract the surface brightness profile along the major axis out to 300 kpc with fixed ellipticity and position

[20] STSDAS is a product of the Space Telescope Science Institute, which is operated by AURA for NASA.

angle, and correct them for Galactic extinction. Error bars on the surface brightness and $g-r$ color profiles are calculated by combining the uncertainty in intensity from the ELLIPSE procedure and the intrinsic fluctuation of the background level obtained from aggressively masked Dragonfly images. The g-band surface brightness and $g-r$ color profiles of NGC 4889 and NGC 4874 are shown in Figure 9. The g-band surface brightness predicted by the best-fit model spectra obtained by spatially stacking spectra in the first two plates, the third and fourth plates, the fifth and sixth plates, and three ICL regions are shown as comparisons. The results from two methods are consistent with each other within 1σ. Figure 9 also shows that the $g-r$ color of three ICL regions inferred from the best-fit alf model are consistent with photometry from Dragonfly images. Both BCG+ICL $g-r$ colors become bluer with increasing radius. This is consistent with our spectroscopic results indicating that the stellar population is more metal-poor with increasing radius.

4.3. Radial Variations

In this section, we compare the radial variations in the stellar population properties. We first compare the median spatially stacked spectra among the central region of NGC 4889 and NGC 4874 (first and second plates), at around 0.5–1R_e (third and fourth plates) and 1–2R_e (fifth and sixth plates), and the ICL regions in Figure 8. Stacked spectra in Figure 8 are smoothed by a 3 pixel wide boxcar kernel, overplotted by the best-fit model spectra. The absorption features in the ICL spectra are visually shallower than the inner regions of BCGs, suggesting a higher velocity dispersion of stars in the ICL.

The g-band image surface brightness profiles and $g-r$ color profiles derived from the Dragonfly images are shown in the top panels of Figure 9. We then compare the stellar population properties as a function of radius in the lower four panels of Figure 9, including their recession velocity (cz), velocity dispersion (σ), stellar age, and iron abundance [Fe/H]. We also include the radial trends of three massive ETGs in the Coma cluster observed in the Deep Coma program: NGC 4860, NGC 4841A, and NGC 4839. The radial coverages of these three galaxies are ∼0–30 kpc. The mean recession velocities of the three ICL regions are very close to their nearest BCGs, NGC 4889 and NGC 4874.

For the velocity dispersion (σ), stellar age, and iron abundance [Fe/H], a clearer view of the radial trends can be found in Figure 10. To study the spatial distribution of stellar population parameters from the central regions of BCGs to the ICL, we make use of the MaNGA data cube that is rectified spatially in units of 0.″5 spatial pixels (spaxels) for the observations of NGC 4889 and NGC 4874 in the first four plates, corresponding to the central regions of the two BCGs, 0.5R_e of NGC 4874, and 1R_e of NGC 4889. Spectra in adjacent spaxels are binned by Voronoi tessellation (Cappellari & Copin 2003). To control the bin size, the S/N ratios achieved in each bin in the central regions of two BCGs are 210 Å^{-1} and 180 Å^{-1} for NGC 4889 and NGC 4874, respectively. The S/N ratios achieved in each bin of the data cube on 1R_e of NGC 4889 and 0.5R_e of NGC 4874 are 120 Å^{-1} and 100 Å^{-1}, respectively. For the 2R_e of NGC 4889 and 1R_e of NGC 4874, we use the "mgCFrame" files and spatially stack all science fibers in the bundles, achieving an S/N ≈ 50 Å^{-1}. The 2D spatial distributions of the best-fit σ, age, and [Fe/H] are displayed in Figure 10.

Both BCGs+ICL structures have rising velocity dispersion profiles, suggesting that stars in the ICL trace the potential of the Coma cluster instead of any individual galaxy. The stellar ages for the three massive galaxies and two BCG+ICL structures are generally old, from the center to the outskirts. This is consistent with previous observations of nearly flat stellar age profiles in ETGs (Sánchez-Blázquez et al. 2007; Greene et al. 2015; Gu et al. 2018a). The stellar age profiles show that both the *in situ* and *ex situ* components of the massive ETGs in Coma have old stellar populations. The result highlights the effect of "environmental quenching" (Peng et al. 2010) and is consistent with the "coordinated assembly" picture in Gu et al. (2018a), in which the massive ETGs in the central regions of galaxy clusters grow by accreting preferentially old stellar systems. In the bottom right panel of Figure 9, we see declining [Fe/H] radial profiles for all of the three massive galaxies and both BCG+ICL structures. In general, the [Fe/H] in the ICL regions are even more metal-poor than the outskirts of BCGs at 1–2R_e. We compare the radial profile in the outskirts of two BCG+ICL structures in our sample with the prediction from the Illustris simulations (Cook et al. 2016). The black dashed line in this panel shows the shifted mean projected profiles of [Z/H] in $z=0$ galaxies that are in the stellar mass bins of $\log(M_*/M_\odot) \in [11.5, 12.0)$. Note that we shift the mean profile since we are comparing only the gradients in the outskirts, and we need to account for the difference between the total metallicity in the simulation and the [Fe/H] in observations. The mean projected profiles of [Z/H] in the Illustris simulations are shifted down by 0.15 dex to match the [Fe/H] at 10 kpc. This difference accounts for the difference between totally metallicity and [Fe/H].

4.4. Combined Constraints from Spectra and Photometry

The broadband $g-r$ color obtained from the Dragonfly Telephoto Array is used as an additional constraint to the stellar age and [Fe/H]. We measure the color from the Dragonfly data within an aperture of $D=32''$, similar to the regions of our stacked spectra. The measured $g-r$ colors are corrected for Galactic extinction. They are 0.58 ± 0.04, 0.56 ± 0.04, and 0.60 ± 0.04 mag for ICL1, ICL2, and ICL3, respectively. We assume the probability density of the observed $g-r$ colors to be a normal distribution and take the measured color and uncertainty as the mean and standard deviation. The color distributions from Dragonfly photometry are shown in green in the top panels of Figure 11. Normalized 1D posterior distributions of the $g-r$ color derived from fitting the continuum-normalized spectra are shown in the top panels in blue. The differences are within 1σ photometric uncertainty. The broadband $g-r$ color provides an independent constraint on the parameter space. We reweight the posterior distributions based on the probability density of the broadband $g-r$ color. More specifically, we assign weights to the Markov chains based on the probability density of the broadband $g-r$ color, and generate new posterior distributions via bootstrap resampling. The middle and bottom panels of Figure 11 show the joint posterior distributions of log(age/Gyr) and [Fe/H] in red, respectively. Slightly tighter constraints are achieved for ICL1 and ICL3. The jointly constrained stellar ages of ICL1, ICL2, and ICL3 are $12.7^{+1.0}_{-3.4}$, $6.7^{+2.9}_{-2.1}$, and $9.7^{+3.5}_{-3.5}$ Gyr, while the jointly constrained [Fe/H] are $-0.97^{+0.21}_{-0.25}$, $-0.63^{+0.28}_{-0.45}$, and $-0.84^{+0.33}_{-0.36}$, respectively. Note that derived parameters only change in the case of the stellar age of ICL2. We note that the

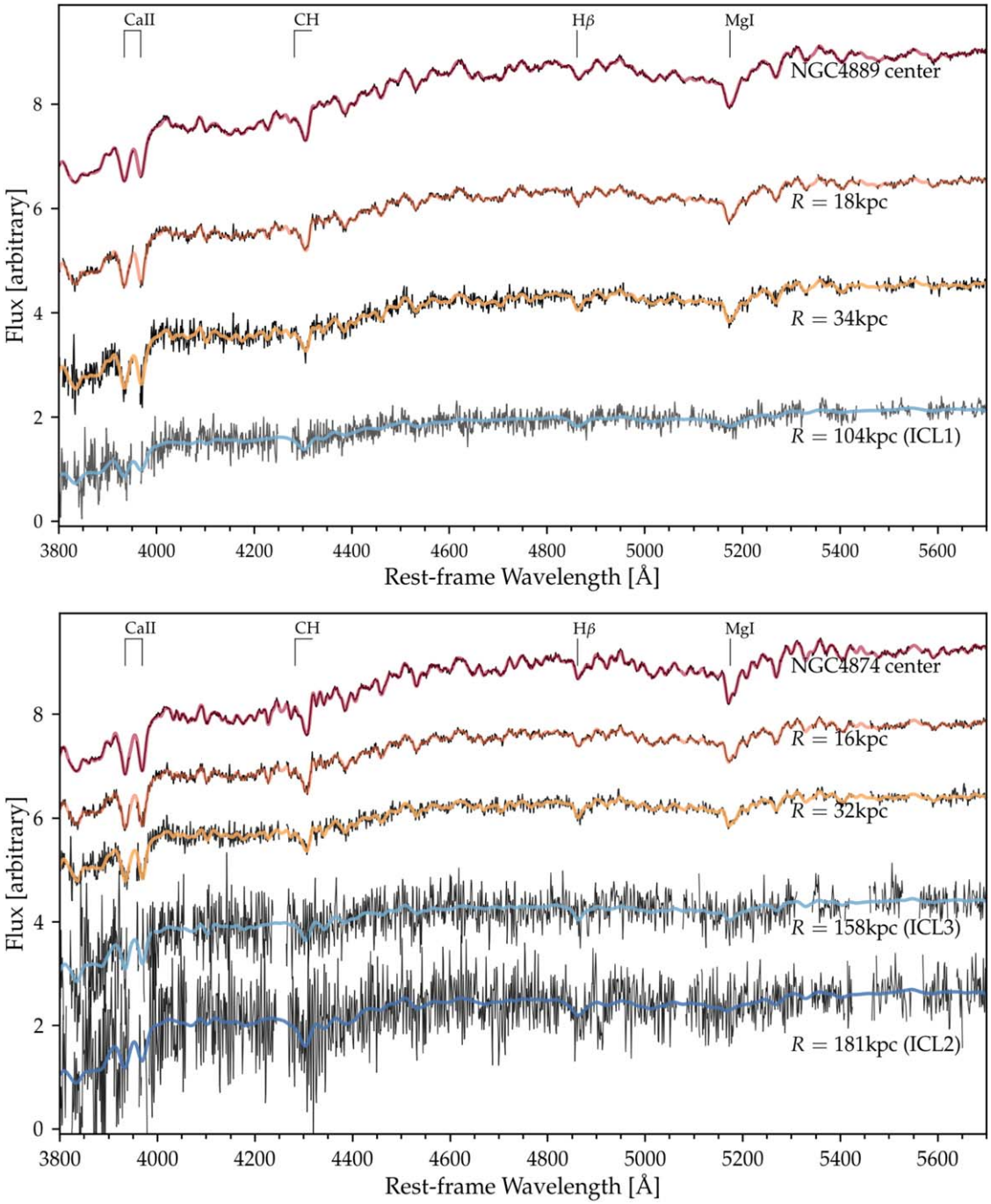

Figure 8. Normalized median stacked spectra (black) at different distances to the centers of NGC 4889 (top panel) and NGC 4874 (bottom). Strong absorption features are labeled. Best-fit model spectra with parameters at minimum χ^2 are shown in colors.

broadband photometry and MaNGA spectra provide two independent constraints on the stellar population parameters. Both data could suffer from systematics in different ways. The changes in the ICL2 colors shows that the two independent methods jointly provide a tighter constraint on the stellar age.

4.5. Dynamical Structure

The Coma cluster is known to have a complex structure (Fitchett & Webster 1987; Mellier et al. 1988). Previous works found major substructures around the bright galaxy NGC 4839, indicating that there is continuing infall at the present day (Fitchett & Webster 1987; Colless & Dunn 1996; Neumann et al. 2001, 2003). Furthermore, the core of the cluster comprises two giant cD galaxies, NGC 4889 and NGC 4874, and X-ray observations (Adami et al. 2005) suggest that these galaxies are likely associated with two distinct substructures. The line-of-sight velocity distributions of intracluster planetary nebulae in the central region of Coma (Gerhard et al. 2007) also suggest an ongoing merger of distinct substructures associated with NGC 4889 and NGC 4874. Our results contribute to this picture with direct kinematic evidence that the core of Coma is, in fact, a double cluster with two distinct virialized components. The high velocity dispersions in the three ICL regions indicate that the stars in the ICL trace the gravitational potential of subclusters, not galaxies. However, the recession

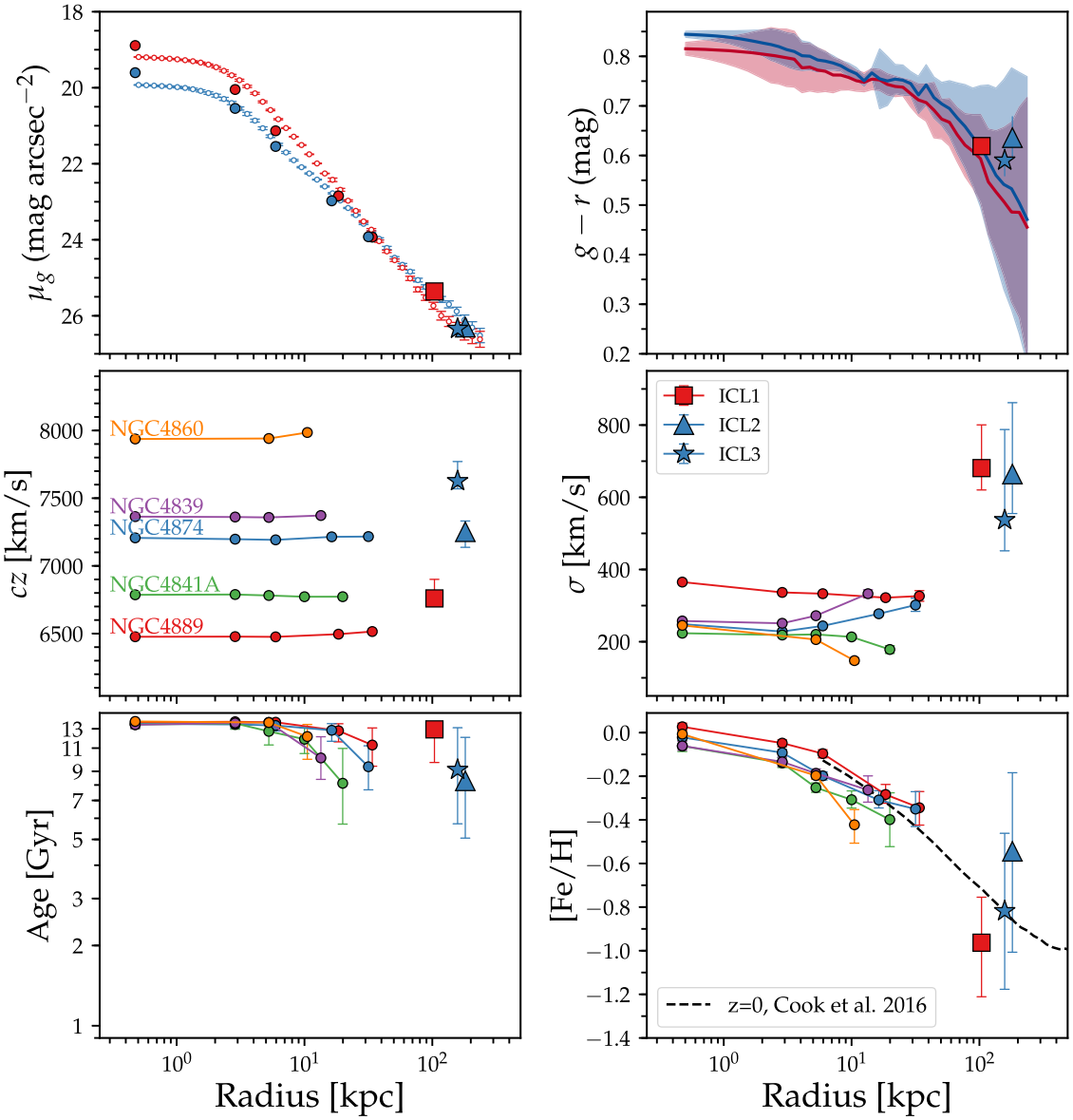

Figure 9. Top panels: g-band surface brightness profiles and $g-r$ color profiles for NGC 4889 (red) and NGC 4874 (blue), extended into the ICL regime. Middle panels: best-fit recessional velocity cz and velocity dispersion σ as a function of radius. Bottom panels: best-fit stellar age and [Fe/H] as a function of radius. Error bars enclose 16th and 84th percentile of the posteriors. Results for ICL regions are marked with the same color as that for their closest BCGs. Dashed line in bottom right panel represents the shifted mean metallicity [Z/H] profile at $z = 0$ of galaxies in the stellar mass bin $11.5 \leqslant \log(M_*/M_\odot) < 12.0$ from the Illustris simulations (Cook et al. 2016). We only compare the gradients in the outskirts and we need to account for the difference between the total metallicity in the simulation and the [Fe/H] in observations, so the profile is shifted down by 0.15 dex.

velocities are consistent with those of the two BCGs, with the difference in velocity between ICL1 and ICL2/ICL3 being $\Delta cz \approx 560$–$850\,\mathrm{km\,s^{-1}}$. This shows that stars in ICL1 are tracing a massive dark matter halo around NGC 4889, while stars in ICL2 and ICL3 are tracing a distinct halo around NGC 4874. Our results confirm that NGC 4889 and NGC 4874 not only originate in separate clusters, but that those clusters are still distinct at the present day.

5. Discussion

The stellar population in the outskirts of galaxies and the ICL contains important clues related to galaxy accretion and dynamical evolution. Simulations predict that *ex situ* mergers are a major contributor to the diffuse light component, and their contribution to the outskirts and ICL regions are more significant for more massive galaxies (Lackner et al. 2012; Cooper et al. 2013; Qu et al. 2017). For example, the IllustrisTNG simulations (Pillepich et al. 2018) predict that a large fraction of stars (>50%) in the outskirts of massive ETGs (>30 kpc) are formed *ex situ*. This fraction is even larger (∼90%) for stars beyond 100 kpc. The radial profile of surface brightness and metallicity of galaxies provide important clues to their accretion histories. For example, tidally stripped stars at large radii are expected to flatten metallicity and surface brightness profiles (Di Matteo et al. 2009; Genel et al. 2014; Vogelsberger et al. 2014; Cook et al. 2016). Cook et al. (2016) show that, in the Illustris Simulations, the radial profiles of metallicity and surface brightness flatten from $z = 1$ to the current epoch, due to the accretion of stars into the outskirts of galaxies. We compare radial trends of the Coma BCG+ICL structures with the simulations. Despite the large uncertainties

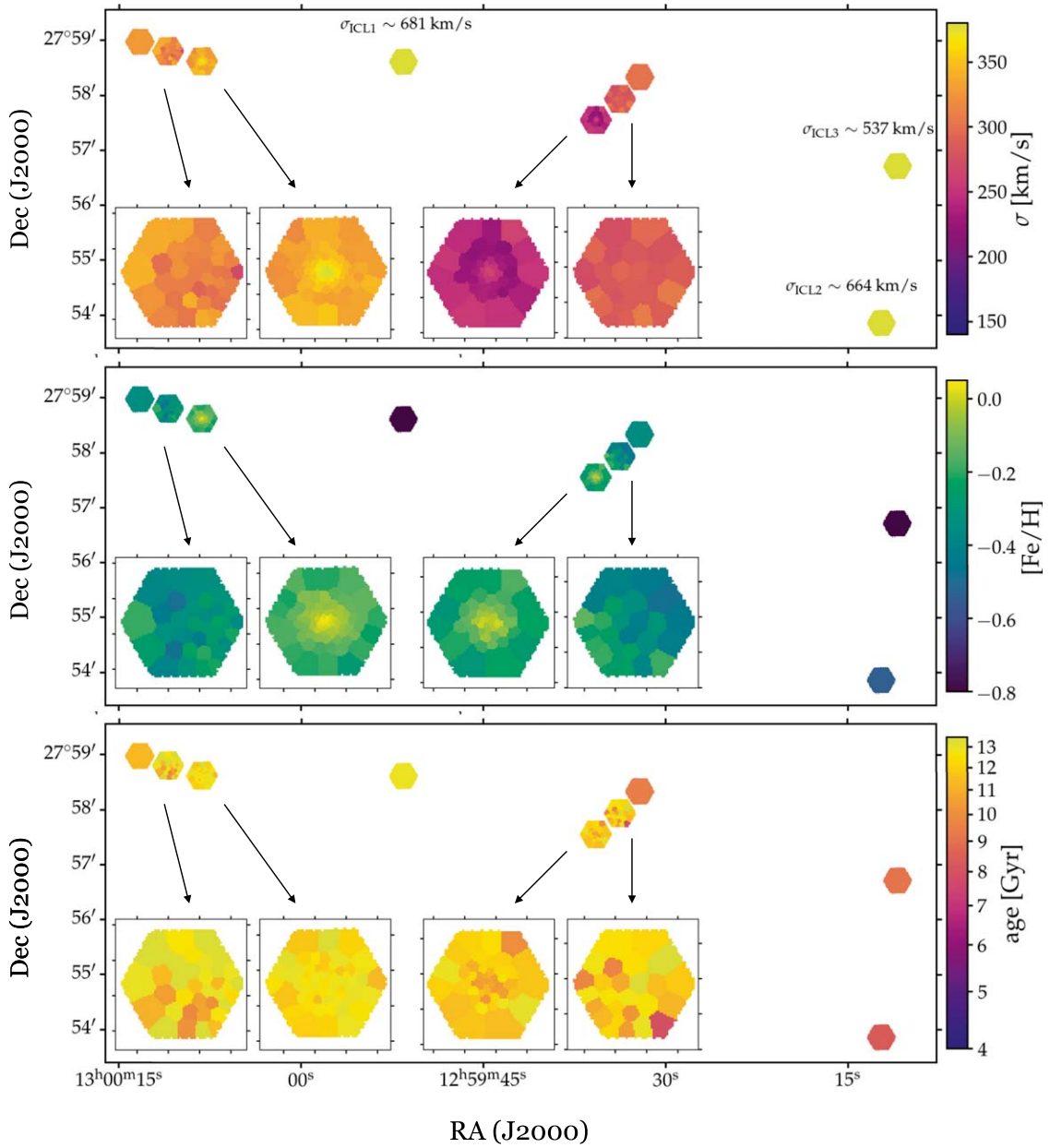

Figure 10. Spatial distributions of stellar velocity dispersion σ (top), iron abundance [Fe/H] (middle), and stellar age (bottom). Spectra in adjacent spaxels are binned by Voronoi tessellation.

of metallicity in the ICL regions, the radial of [Fe/H] trends at 100–200 kpc is consistent with the prediction from simulations.

If the light at 100–200 kpc is indeed dominated by *ex situ* components as predicted by the simulations (e.g., Pillepich et al. 2018), stellar populations in the ICL regions can shed light on the progenitors of ICL. ETGs experienced complex assembly histories. However, they obey tight scaling relations, including the relation between the stellar mass and stellar metallicity, which provide important clues to their star formation and chemical enrichment history (Kirby et al. 2013; Ma et al. 2016; Lu et al. 2017). By comparing the [Fe/H] of ICL with the [Fe/H] of ETGs across a wide stellar mass range indicated by the relation between stellar mass and stellar metallicity (MZR), we can infer the possible progenitors of the ICL regions. Figure 12 shows the MZR: we draw a horizontal region across nearly all stellar mass, with the vertical range covering the 18th and 84th percentiles of [Fe/H] in the three ICL regions. The [Fe/H] of the ICL is compared to other populations, including three dwarf elliptical galaxies in the Coma cluster in our sample, ETGs stacked in stellar mass bins (Conroy et al. 2014), star-forming galaxies in SDSS (Zahid et al. 2017), and the MZR from Gallazzi et al. (2005), which covers both star-forming and quiescent SDSS galaxies as well as dwarf galaxies in the Local Group (Kirby et al. 2013). Data points from Gallazzi et al. (2005) and Zahid et al. (2017) represent the total metallicity instead of iron abundances. Note that, for the more massive galaxies, the figure shows the relation between their stellar mass and [Fe/H] or total metallicity in the inner region.

The [Fe/H] of ICL regions is similar to the [Fe/H] of three dwarf elliptical galaxies in the Coma cluster. If we estimate the stellar mass of the ICL progenitors based on the MZR, and assume the progenitors have early truncated star formation

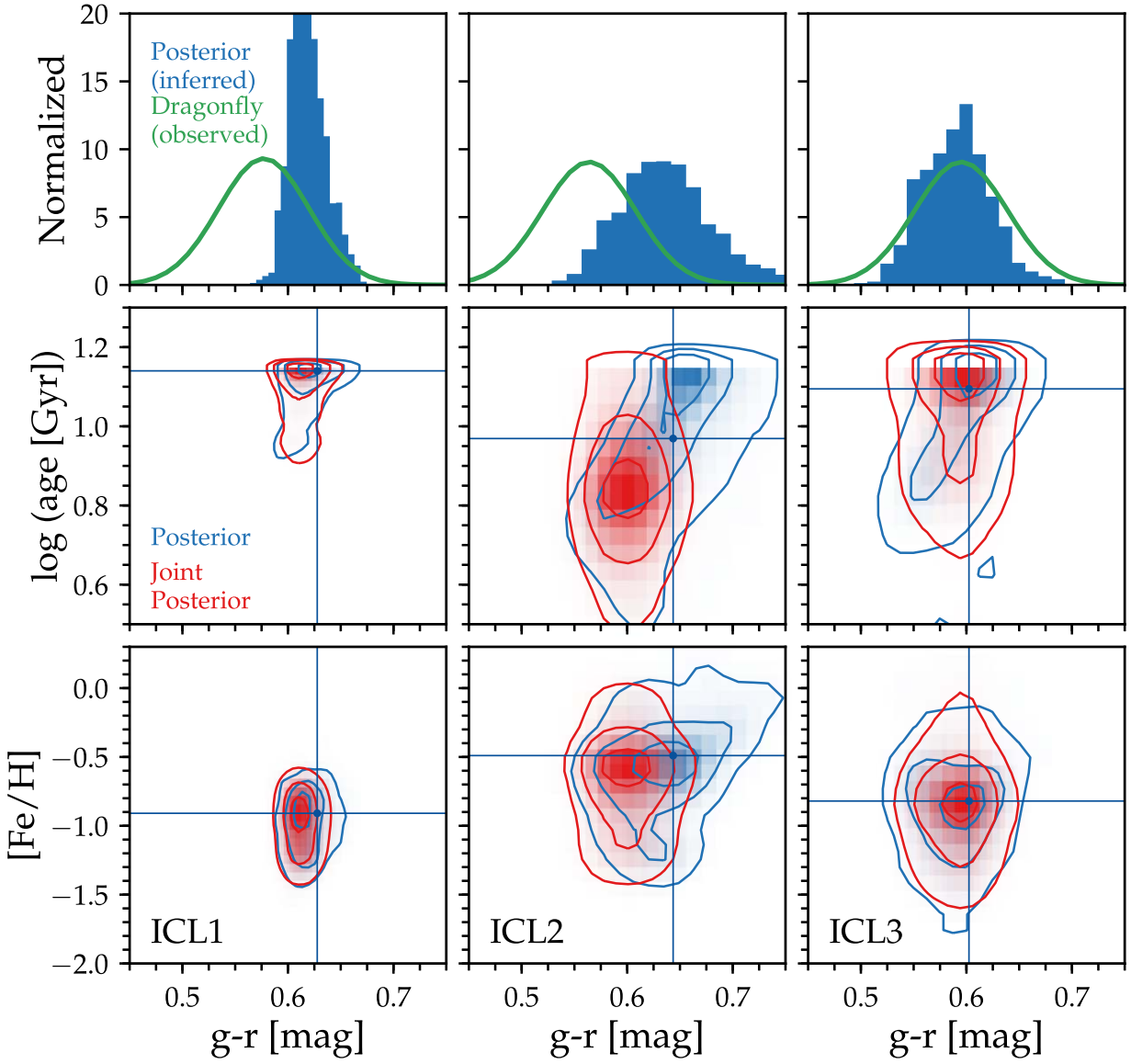

Figure 11. Top panel: 1D histogram of inferred $g - r$ color posterior from `alf` (blue) for ICL1 (left), ICL2 (middle), and ICL3 (right), compared with the $g - r$ color from broadband images taken by the Dragonfly Telephoto Array (green). Middle and bottom panels: projections of the posterior of log(age), [Fe/H] and $g - r$ in 2D histograms. Blue lines show the best-fit parameters at $\chi^2_{\rm min}$. Joint posterior distributions from combining broadband colors and model spectra colors are shown in the same panels in red.

histories as indicated by the stellar age of the three ICL regions, the stellar mass of possible progenitors covers a range from $\sim 10^8\,M_\odot$ to $3 \times 10^9\,M_\odot$. We can further estimate the stellar mass of the ICL. We first estimate the luminosity of the annular regions centered on NGC 4889 and NGC 4874 between radii of 100 and 200 kpc. We use the r-band surface brightness profiles measured on the Dragonfly image to calculate the luminosity. We then make use of the mean $(M/L)_r$ measured on the ICL spectra, which is $\sim 2\,M_\odot/L_\odot$. Assuming little spatial variation with the $(M/L)_r$, the stellar mass of the ICL is $\sim 10^{12}\,M_\odot$. Therefore, the BCGs would need to merge with 3×10^3–10^4 such dwarf galaxies if they are the only contributors. Considering that we are making a comparison with the [Fe/H] in the galaxy centers, and their outskirts in general have lower [Fe/H], it is likely that the stars of the ICL come partly from the outskirts of more massive galaxies. Therefore, the buildup of ICL could be from partial tidal stripping of massive galaxies and/or from the disruption of dwarf galaxies with stellar mass above $\sim 10^8\,M_\odot$. However, it is unlikely that the ICL forms directly from major mergers of massive galaxies.

We checked whether our results are robust against possible background contamination. As shown in Figure 1, the ICL regions are selected based on deep Dragonfly images and are away from contamination. We further made use of the high-resolution optical images from the Advanced Camera for Surveys (ACS) on the Hubble Space Telescope. Data are observed in programs 10861 and 11711. ICL1 regions are completely covered, and ICL2 and ICL3 are only half-covered. For ICL1, we have tried to remove fibers close to relatively bright background objects identified from the ACS images. More specifically, we have performed Source Extractor (Bertin & Arnouts 1996) on the ACS image to identify relatively bright sources above 5σ in flux. We tried to exclude fibers locate within $1\farcs2$ of the contamination. We select the uncontaminated fibers in the same way for all exposures, and fit the stacked

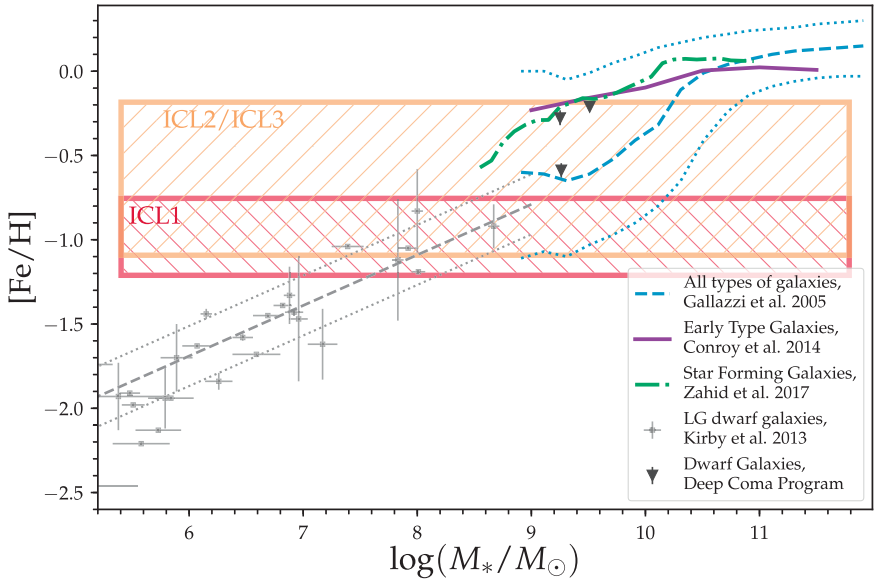

Figure 12. Relation between stellar mass and [Fe/H] for three dwarf elliptical galaxies in the Coma cluster (triangles), and previous results from the literature: gray symbols show Local Group dwarf galaxies from Kirby et al. (2013), and gray dashed and dotted lines represent the median, 16th, and 84th percentiles of the metallicity distributions. Blue dashed and dotted lines show the median, 16th, and 84th percentiles of the metallicity distributions for various types of galaxies in Gallazzi et al. (2005). Purple line shows the stellar mass–metallicity relation for early-type galaxies binned in stellar mass (Conroy et al. 2014). Green line represents the relation for star-forming galaxies in SDSS (Zahid et al. 2017). For the three ICL regions in the Coma cluster without stellar mass constraints, their median, 16th, and 84th percentiles of [Fe/H] are shown as horizontal region.

spectra. Very similar stellar populations are revealed with and without this exclusion. The changes in recession velocity (cz), velocity dispersion, log(age), and [Fe/H] are all smaller than 28% of 1σ uncertainty. We conclude that the contribution of background source contamination does not impact our results.

The ICL1 spectrum is located between NGC 4889 and NGC 4874. Using a spectral model with a single velocity component, we cannot rule out the possibility that the stellar contents in ICL1 consist of two velocity components, both with lower velocity dispersion. With higher-S/N data, we should be able to fit the spectra with a two-component model to confirm our conclusion.

6. Summary

We have presented the stellar population analysis through full optical spectral modeling for three ICL regions in the Coma cluster that are located between 100 and 200 kpc from their nearest BCGs. We have measured their recession velocities, velocity dispersion, stellar ages, and iron abundances using spectra obtained as part of the Deep Coma Program within the SDSS-IV/MaNGA survey. Based on their line-of-sight velocity and velocity dispersion, the three ICL regions are associated with two distinct subclusters centered on NGC 4889 and NGC 4874. For the BCG+ICL structures, the radial profiles of stellar age are old and flat, and the radial profiles of [Fe/H] decline with increasing radius. The stellar populations in the ICL regions are all old and metal-poor. The [Fe/H] of three ICL regions are slightly more metal-poor compared to the outskirts (10–30 kpc) of massive ETGs in the Coma cluster. From the derived stellar age and metallicity, the buildup of ICL is likely to be either through the accretion of low-mass galaxies that have ended their star formation early on, or else via partial tidal stripping of massive galaxies, instead of major mergers of massive galaxies.

We thank the referee for constructive comments that helped improve this paper. M.G. acknowledges support from the National Science Foundation Graduate Research Fellowship and the Henry Norris Russell Postdoctoral Fellowship. C.C. acknowledges support from NASA grant NNX15AK14G, NSF grant AST-1313280, and the Packard Foundation. M.A.B. acknowledges NSF Award AST-1517006. The computations in this paper were run on the Odyssey cluster supported by the FAS Division of Science, Research Computing Group at Harvard University.

Funding for the Sloan Digital Sky Survey IV has been provided by the Alfred P. Sloan Foundation, the U.S. Department of Energy Office of Science, and the Participating Institutions. SDSS-IV acknowledges support and resources from the Center for High-Performance Computing at the University of Utah. The SDSS website is www.sdss.org.

SDSS-IV is managed by the Astrophysical Research Consortium for the Participating Institutions of the SDSS Collaboration including the Brazilian Participation Group, the Carnegie Institution for Science, Carnegie Mellon University, the Chilean Participation Group, the French Participation Group, Harvard-Smithsonian Center for Astrophysics, Instituto de Astrofísica de Canarias, The Johns Hopkins University, Kavli Institute for the Physics and Mathematics of the Universe (IPMU)/University of Tokyo, Lawrence Berkeley National Laboratory, Leibniz Institut für Astrophysik Potsdam (AIP), Max-Planck-Institut für Astronomie (MPIA Heidelberg), Max-Planck-Institut für Astrophysik (MPA Garching), Max-Planck-Institut für Extraterrestrische Physik (MPE), National Astronomical Observatories of China, New Mexico State University, New York University, University of Notre Dame, Observatário

Nacional/MCTI, The Ohio State University, Pennsylvania State University, Shanghai Astronomical Observatory, United Kingdom Participation Group, Universidad Nacional Autónoma de México, University of Arizona, University of Colorado Boulder, University of Oxford, University of Portsmouth, University of Utah, University of Virginia, University of Washington, University of Wisconsin, Vanderbilt University, and Yale University.

Appendix

In this Appendix, we examine our ability to recover the recessional velocity, velocity dispersion, age, and overall metallicity for ICL-like spectra with `alf`. The ICL presents a few related unique challenges due to the low S/N and very high velocity dispersions.

We begin by exploring the effect of the continuum normalization on the derived parameters. Our default approach is to set the degree of the polynomial as $(\lambda_{max}-\lambda_{min})/100$ Å, which means a tenth-order polynomial in the wavelength range 3800–5700 Å. We test the sensitivity of the results to the polynomial degree in Figure A1. We have constructed a mock spectra data set with ten realizations at a range of S/N from 10 to 100 $Å^{-1}$. We assumed the mock spectra have a true recessional velocity of 7200 km s^{-1}, a velocity dispersion of 800 km s^{-1}, an age of 10 Gyr and a metallicity of $[Z/H] = -0.5$. The data are fit over two wavelength ranges: 4000–4700 Å and 4700–5700 Å. The results are shown in Figure A1 as a function of the highest degree of the polynomial used in fitting the continuum. To test the appropriate order of polynomial term to use, we fit mock spectra with different assumptions of this order, ranging from three to ten. It turns out that this degree is crucial to our results. The velocity dispersion and low metallicity make it difficult to extract absorption features. If a high-order polynomial is used to fit the continuum, real absorption features could be misinterpreted as part of the continuum, thus producing a biased result. As shown in Figure A1, a high-order polynomial slightly biases age and metallicity, especially for low-S/N spectra, and results in larger error bars. The figure shows that the recessional velocity and velocity dispersion can be recovered at good precision for mock spectra at all S/N. The biased recessional velocity from the true value is within 50 km s^{-1}, and the biased velocity dispersions are no more than 20 km s^{-1} different if we adopt a highest degree of polynomial smaller than 6. Even for $S/N \leqslant 20$ mock spectra, age, and [Z/H] can be recovered well if we choose the right degree of polynomial to fit the continuum. In this paper, we choose to use a polynomial with the highest degree of 6 to fit the ICL spectra. The mean biases on age are 0.6 and 0.3 Gyr at $S/N = 10$ $Å^{-1}$ and $S/N = 20$ $Å^{-1}$, and the mean biases on [Z/H] are 0.04 and 0.01 dex, respectively.

The stellar absorption features in the ICL spectra are much shallower compared to typical ETG spectra, due to the higher velocity dispersion of the former (Figure 5). As a consequence, the uncertainties on derived parameters are likely to be higher for the ICL than for ETGs, at a given S/N. We explore this issue in Figure A2, where we show recovered parameters, as well as uncertainties, as a function of S/N for an ETG-like dispersion

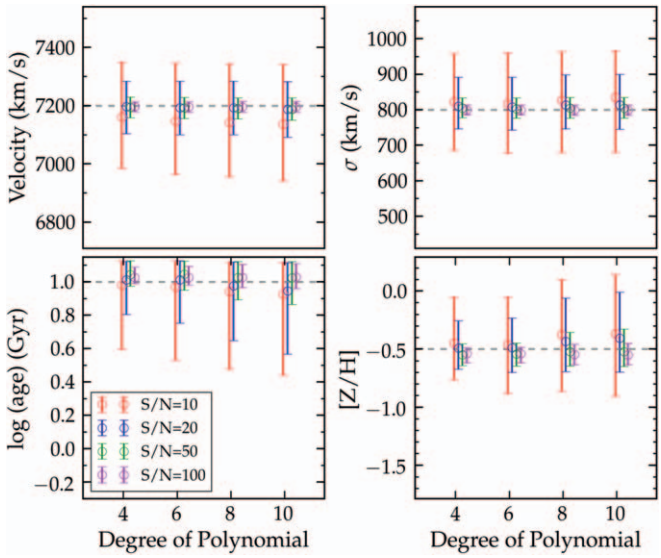

Figure A1. Test of recovery of recessional velocity, velocity dispersion, age, and overall metallicity [Z/H] with high-velocity dispersion mock spectra by tuning the order of polynomial used to fit the continuum. Default degree of the polynomial is $(\lambda_{max}-\lambda_{min})/100$ Å. We constructed 10 realizations at each S/N. Figure shows the mean values of these 10 realizations. Red, blue, green, and purple symbols show parameters at 50th percentile with spectra at S/N of 10, 20, 50, and 100 $Å^{-1}$, respectively. Error bars enclose 16th to 84th percentiles. Gray dashed lines indicate the input values. For ICL spectra, we use a sixth-order polynomial.

(200 km s^{-1}) and an ICL-like dispersion (700 km s^{-1}). In addition, we investigate the case where the S/N is not a constant as a function of wavelength. We construct mock spectra with high (700 km s^{-1}) velocity dispersion, but the S/N blueward 4000 Å is only 60% of that in the redder portion of the wavelength range, which is more similar to the nonuniform S/N in the ICL data. The results are shown in red. The blue symbols represent the case where the S/N of the mock spectra is constant as a function of wavelength. In the lower panels, we also include the actual uncertainties and S/N values for the three ICL regions in the Coma cluster, with S/N of 10–20 $Å^{-1}$, which is similar to the S/N we achieved in the spatially stacked ICL spectra, the uncertainty in [Fe/H] is about 0.1 dex larger than that derived from fitting typical ETG spectra. Although the uncertainties on [Fe/H] and stellar age are similar to the case of uniform S/N, the error constraints on recession velocity and velocity dispersion are worse. The results of the three ICL regions are shown as a comparison. Their error constraints are closer to what we found in the mock data with high velocity dispersion and nonuniform spectra uncertainty. We further conduct an empirical test by randomly selecting half of the ICL1 fibers and constructing 10 such realizations. Results are robust in this test. The median value difference between the measurements on the full and the half sample are less than 35% of one sigma uncertainty in all four parameters. For the low-S/N sample, the uncertainty of [Fe/H] and log(age) is, in general, consistent with prediction from the mock test. Uncertainties on velocity and velocity dispersion are higher than the prediction from the mock data, because data with $1/\sqrt{S/N}$ would suffer more from systematics and background sky emission.

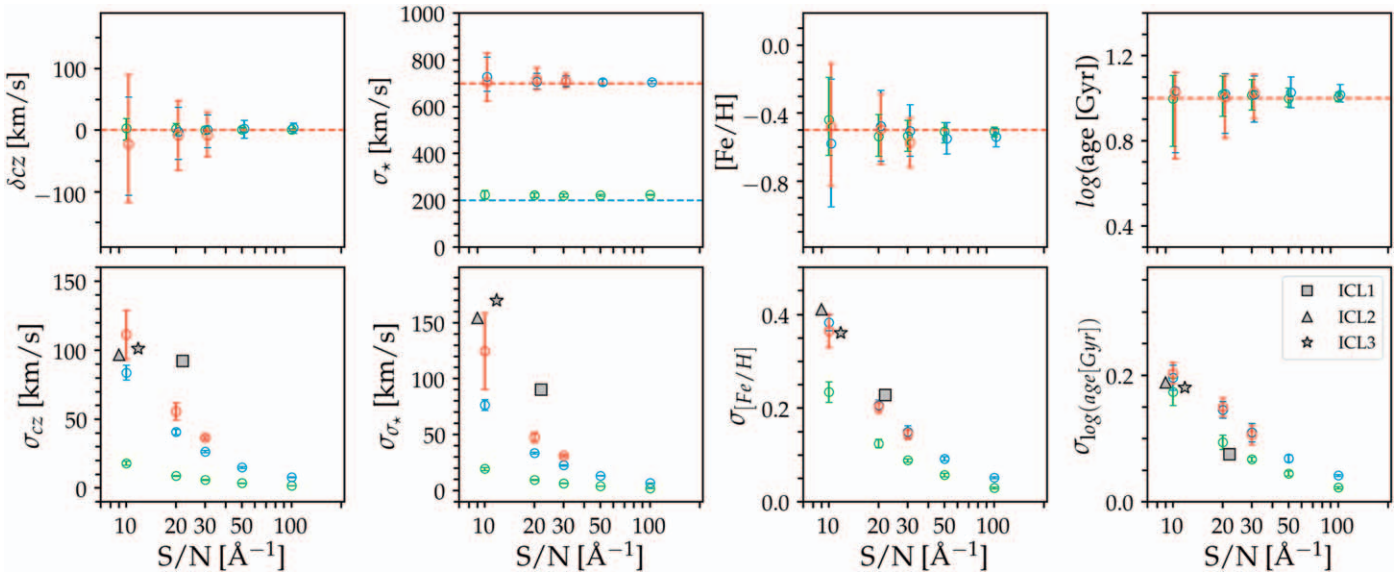

Figure A2. Recovery of parameters using mock spectra of systems with low (200 km s^{-1}, green) and high (700 km s^{-1}, red and blue) velocity dispersion as a function of S/N. We constructed 10 realizations at each S/N. Blue symbols represent the case where the S/N of the mock spectra is a constant as a function of wavelength. Red symbols represent the case where the S/N is not a constant: S/N blueward 4000 Å is 60% of the S/N in rest wavelength range. Top panels: recovered velocity, velocity dispersion, [Fe/H], and stellar age, compared to the input values (dashed lines). Error bars enclose 16th to 84th percentiles. Bottom panels: typical uncertainty on the recovered parameters. For stellar populations with high velocity dispersion (700 km s^{-1}), the recovered parameters have larger error bars. The uncertainties of stellar population parameters from fitting the ICL spectra are compared (gray).

ORCID iDs

Meng Gu https://orcid.org/0000-0002-4267-9344
Charlie Conroy https://orcid.org/0000-0002-1590-8551
David Law https://orcid.org/0000-0002-9402-186X
Pieter van Dokkum https://orcid.org/0000-0002-8282-9888
Renbin Yan https://orcid.org/0000-0003-1025-1711
David Wake https://orcid.org/0000-0002-6047-1010
Kevin Bundy https://orcid.org/0000-0001-9742-3138
Alexa Villaume https://orcid.org/0000-0003-1887-0621
Roberto Abraham https://orcid.org/0000-0002-4542-921X
Allison Merritt https://orcid.org/0000-0001-9467-7298
Jielai Zhang https://orcid.org/0000-0001-5310-4186
Matthew Bershady https://orcid.org/0000-0002-3131-4374
Dmitry Bizyaev https://orcid.org/0000-0002-3601-133X
Niv Drory https://orcid.org/0000-0002-7339-3170
Kaike Pan https://orcid.org/0000-0002-2835-2556

References

Abolfathi, B., Aguado, D. S., Aguilar, G., et al. 2018, ApJS, 235, 42
Abraham, R. G., & van Dokkum, P. G. 2014, PASP, 126, 55
Adami, C., Biviano, A., Durret, F., & Mazure, A. 2005, A&A, 443, 17
Adami, C., Pompei, E., Sadibekova, T., et al. 2016, A&A, 592, A7
Alamo-Martínez, K. A., & Blakeslee, J. P. 2017, ApJ, 849, 6
Arnaboldi, M., Freeman, K. C., Okamura, S., et al. 2003, AJ, 125, 514
Arnaboldi, M., Gerhard, O., Aguerri, J. A. L., et al. 2004, ApJL, 614, L33
Bender, R., Kormendy, J., Cornell, M. E., & Fisher, D. B. 2015, ApJ, 807, 56
Bertin, E., & Arnouts, S. 1996, A&AS, 117, 393
Bezanson, R., van Dokkum, P. G., Tal, T., et al. 2009, ApJ, 697, 1290
Blanton, M. R., Bershady, M. A., Abolfathi, B., et al. 2017, AJ, 154, 28
Bundy, K., Bershady, M. A., Law, D. R., et al. 2015, ApJL, 798, L7
Burke, C., Hilton, M., & Collins, C. 2015, MNRAS, 449, 2353
Calcáneo-Roldán, C., Moore, B., Bland-Hawthorn, J., Malin, D., & Sadler, E. M. 2000, MNRAS, 314, 324
Cappellari, M., & Copin, Y. 2003, MNRAS, 342, 345
Choi, J., Dotter, A., Conroy, C., et al. 2016, ApJ, 823, 102
Coccato, L., Gerhard, O., & Arnaboldi, M. 2010, MNRAS, 407, L26
Coccato, L., Gerhard, O., Arnaboldi, M., & Ventimiglia, G. 2011, A&A, 533, A138
Colless, M., & Dunn, A. M. 1996, ApJL, 458, L435
Conroy, C., Graves, G. J., & van Dokkum, P. G. 2014, ApJL, 780, L33
Conroy, C., & van Dokkum, P. 2012, ApJL, 747, L69
Conroy, C., van Dokkum, P. G., & Villaume, A. 2017, ApJ, 837, 166
Conroy, C., Villaume, A., van Dokkum, P. G., & Lind, K. 2018, ApJ, 854, 139
Conroy, C., Wechsler, R. H., & Kravtsov, A. V. 2007, ApJ, 668, 826
Contini, E., De Lucia, G., Villalobos, Á, & Borgani, S. 2014, MNRAS, 437, 3787
Contini, E., Yi, S. K., & Kang, X. 2018, MNRAS, 479, 932
Cook, B. A., Conroy, C., Pillepich, A., Rodriguez-Gomez, V., & Hernquist, L. 2016, ApJ, 833, 158
Cooper, A. P., D'Souza, R., Kauffmann, G., et al. 2013, MNRAS, 434, 3348
Daddi, E., Renzini, A., Pirzkal, N., et al. 2005, ApJ, 626, 680
Dekel, A., Sari, R., & Ceverino, D. 2009, ApJ, 703, 785
Di Matteo, P., Pipino, A., Lehnert, M. D., Combes, F., & Semelin, B. 2009, A&A, 499, 427
Dressler, A. 1979, ApJL, 231, L659
Drory, N., MacDonald, N., Bershady, M. A., et al. 2015, AJ, 149, 77
Duc, P.-A., Cuillandre, J.-C., Karabal, E., et al. 2015, MNRAS, 446, 120
Edwards, L. O. V., Alpert, H. S., Trierweiler, I. L., Abraham, T., & Beizer, V. G. 2016, MNRAS, 461, 230
Faber, S. M., Burstein, D., & Dressler, A. 1977, AJ, 82, 941
Feldmann, R., Carollo, C. M., Mayer, L., et al. 2010, ApJ, 709, 218
Feldmeier, J. J., Mihos, J. C., Morrison, H. L., et al. 2004, ApJ, 609, 617
Fitchett, M., & Webster, R. 1987, ApJ, 317, 653
Foreman-Mackey, D. 2016, JOSS, 1, 24
Foreman-Mackey, D., Hogg, D. W., Lang, D., & Goodman, J. 2013, PASP, 125, 306
Foster, C., Proctor, R. N., Forbes, D. A., et al. 2009, MNRAS, 400, 2135
Gallazzi, A., Charlot, S., Brinchmann, J., White, S. D. M., & Tremonti, C. A. 2005, MNRAS, 362, 41
Geller, M. J., Diaferio, A., & Kurtz, M. J. 1999, ApJL, 517, L23
Genel, S., Vogelsberger, M., Springel, V., et al. 2014, MNRAS, 445, 175
Gerhard, O., Arnaboldi, M., Freeman, K. C., et al. 2007, A&A, 468, 815
Giallongo, E., Menci, N., Grazian, A., et al. 2014, ApJ, 781, 24
Gonzalez, A. H., Zabludoff, A. I., & Zaritsky, D. 2005, ApJ, 618, 195
Greene, J. E., Janish, R., Ma, C.-P., et al. 2015, ApJ, 807, 11
Greene, J. E., Murphy, J. D., Comerford, J. M., Gebhardt, K., & Adams, J. J. 2012, ApJ, 750, 32
Gregg, M. D., & West, M. J. 1998, Natur, 396, 549
Gu, M., Conroy, C., & Brammer, G. 2018a, ApJL, 862, L18

Gu, M., Conroy, C., Law, D., et al. 2018b, ApJ, 859, 37
Guennou, L., Adami, C., Da Rocha, C., et al. 2012, A&A, 537, A64
Gunn, J. E., Siegmund, W. A., Mannery, E. J., et al. 2006, AJ, 131, 2332
Hopkins, P. F., Hernquist, L., Cox, T. J., Dutta, S. N., & Rothberg, B. 2008, ApJ, 679, 156
Huang, S., Ho, L. C., Peng, C. Y., Li, Z.-Y., & Barth, A. J. 2016, ApJ, 821, 114
Huang, S., Leauthaud, A., Greene, J., et al. 2018a, MNRAS, 480, 521
Huang, S., Leauthaud, A., Greene, J. E., et al. 2018b, MNRAS, 475, 3348
Hyde, J. B., & Bernardi, M. 2009, MNRAS, 394, 1978
Jedrzejewski, R. I. 1987, MNRAS, 226, 747
Johansson, P. H., Naab, T., & Ostriker, J. P. 2012, ApJ, 754, 115
Kelson, D. D., Zabludoff, A. I., Williams, K. A., et al. 2002, ApJL, 576, L720
Kirby, E. N., Cohen, J. G., Guhathakurta, P., et al. 2013, ApJ, 779, 102
Kroupa, P. 2001, MNRAS, 322, 231
Kurucz, R. L. 1993, SYNTHE spectrum synthesis programs and line data CD-ROM (Cambridge, MA: Smithsonian Astrophysical Observatory)
Kurucz, R. L. 1970, SAOSR, 309, 1
Lackner, C. N., Cen, R., Ostriker, J. P., & Joung, M. R. 2012, MNRAS, 425, 641
Law, D. R., Cherinka, B., Yan, R., et al. 2016, AJ, 152, 83
Law, D. R., Yan, R., Bershady, M. A., et al. 2015, AJ, 150, 19
Liu, M. C., & Graham, J. R. 2001, ApJ, 557, 31
Longobardi, A., Arnaboldi, M., Gerhard, O., & Mihos, J. C. 2015, A&A, 579, L3
Lu, Y., Benson, A., Wetzel, A., et al. 2017, ApJ, 846, 66
Ma, X., Hopkins, P. F., Kasen, D., et al. 2016, MNRAS, 459, 3614
Mellier, Y., Mathez, G., Mazure, A., Chauvineau, B., & Proust, D. 1988, A&A, 199, 67
Mihos, J. C., Harding, P., Feldmeier, J., & Morrison, H. 2005, ApJL, 631, L41
Mobasher, B., Bridges, T. J., Carter, D., et al. 2001, ApJS, 137, 279
Montes, M., & Trujillo, I. 2014, ApJ, 794, 137
Montes, M., & Trujillo, I. 2018, MNRAS, 474, 917
Murante, G., Giovalli, M., Gerhard, O., et al. 2007, MNRAS, 377, 2
Naab, T., Johansson, P. H., Ostriker, J. P., & Efstathiou, G. 2007, ApJ, 658, 710
Navarro-González, J., Ricciardelli, E., Quilis, V., & Vazdekis, A. 2013, MNRAS, 436, 3507
Neumann, D. M., Arnaud, M., Gastaud, R., et al. 2001, A&A, 365, L74
Neumann, D. M., Lumb, D. H., Pratt, G. W., & Briel, U. G. 2003, A&A, 400, 811
Oser, L., Naab, T., Ostriker, J. P., & Johansson, P. H. 2012, ApJ, 744, 63
Oser, L., Ostriker, J. P., Naab, T., Johansson, P. H., & Burkert, A. 2010, ApJ, 725, 2312
Ostriker, J. P., & Tremaine, S. D. 1975, ApJL, 202, L113
Peng, Y.-j., Lilly, S. J., Kovac, K., et al. 2010, ApJL, 721, L193
Pillepich, A., Nelson, D., Hernquist, L., et al. 2018, MNRAS, 475, 648
Puchwein, E., Springel, V., Sijacki, D., & Dolag, K. 2010, MNRAS, 406, 936
Purcell, C. W., Bullock, J. S., & Zentner, A. R. 2007, ApJ, 666, 20
Qu, Y., Helly, J. C., Bower, R. G., et al. 2017, MNRAS, 464, 1659
Rines, K., Geller, M. J., Diaferio, A., & Kurtz, M. J. 2013, ApJL, 767, L15
Rodriguez-Gomez, V., Pillepich, A., Sales, L. V., et al. 2016, MNRAS, 458, 2371
Rudick, C. S., Mihos, J. C., Frey, L. H., & McBride, C. K. 2009, ApJ, 699, 1518
Rudick, C. S., Mihos, J. C., Harding, P., et al. 2010, ApJ, 720, 569
Sánchez-Blázquez, P., Forbes, D. A., Strader, J., Brodie, J., & Proctor, R. 2007, MNRAS, 377, 759
Sánchez-Blázquez, P., Peletier, R. F., Jiménez-Vicente, J., et al. 2006, MNRAS, 371, 703
Schlafly, E. F., & Finkbeiner, D. P. 2011, ApJ, 737, 103
Smee, S. A., Gunn, J. E., Uomoto, A., et al. 2013, AJ, 146, 32
Sohn, J., Geller, M. J., Zahid, H. J., et al. 2016, ApJS, 229, 20
Spolaor, M., Kobayashi, C., Forbes, D. A., Couch, W. J., & Hau, G. K. T. 2010, MNRAS, 408, 272
Toledo, I., Melnick, J., Selman, F., et al. 2011, MNRAS, 414, 602
Trujillo, I., Feulner, G., Goranova, Y., et al. 2006, MNRAS, 373, L36
van der Wel, A., Franx, M., van Dokkum, P. G., et al. 2014, ApJ, 788, 28
van der Wel, A., Rix, H.-W., Wuyts, S., et al. 2011, ApJ, 730, 38
van Dokkum, P. G., Abraham, R., & Merritt, A. 2014, ApJL, 782, L24
van Dokkum, P. G., Whitaker, K. E., Brammer, G., et al. 2010, ApJ, 709, 1018
Veale, M., Ma, C.-P., Greene, J. E., et al. 2018, MNRAS, 473, 5446
Villaume, A., Conroy, C., Johnson, B., et al. 2017, ApJS, 230, 23
Vogelsberger, M., Genel, S., Springel, V., et al. 2014, MNRAS, 444, 1518
Wake, D. A., Bundy, K., Diamond-Stanic, A. M., et al. 2017, AJ, 154, 86
White, S. D. M., & Rees, M. J. 1978, MNRAS, 183, 341
Williams, B. F., Ciardullo, R., Durrell, P. R., et al. 2007, ApJ, 656, 756
Yan, R., Bundy, K., Law, D. R., et al. 2016, AJ, 152, 197
Yan, R., Tremonti, C., Bershady, M. A., et al. 2016, AJ, 151, 8
Zahid, H. J., Kudritzki, R.-P., Conroy, C., Andrews, B., & Ho, I.-T. 2017, ApJ, 847, 18
Zibetti, S., White, S. D. M., Schneider, D. P., & Brinkmann, J. 2005, MNRAS, 358, 949
Zwicky, F. 1951, PASP, 63, 61